Stretchable all-gel organic electrochemical transistors

Linlin Lu, Xu Liu, Puzhong Gu, Zhenyu Hu, Xing Liang ⬤, Zhiying Deng, Zejun Sun, Xiaoyu Zhang ⬤, Xiao Yang, Jie Yang ✉, Guoqing Zu ⬤ ✉ & Jia Huang ⬤ ✉

Stretchable organic electrochemical transistors (OECTs) are promising for flexible electronics. However, the balance between stretchability and electrical properties is a great challenge for OECTs. Here, high-performance stretchable all-gel OECTs based on semiconducting polymer gel active layers and poly(ionic liquid) ionogel electrolytes are developed. The all-gel network structures effectively promote ion penetration/transport and endows the OECTs with high stretchability. The resulting OECTs exhibit an excellent combination of ultra-high transconductance of 86.4 mS, on/off ratio of 1.2×10^5, stretchability up to 50%, and high stretching stability up to 10000 cycles under 30% strain. We demonstrate that the all-gel OECTs can be used as stretchable pressure-sensitive electronic skins with a low detection limit for tactile perception of robotic hands. In addition, the all-gel OECTs can be applied as stretchable artificial synapses for neuromorphic simulation and highly sensitive stretchable gas sensors for simulating olfactory perception process and monitoring food quality. This work provides a general all-gel strategy toward high-performance flexible electronics.

With the continuous development of electronic technology, stretchable and wearable electronics are urgently needed to meet the increasing demand for electronic skins, soft robots, human-machine interfaces, and biomedical monitoring[1-3]. Stretchable organic electrochemical transistors (OECTs), as an emerging electronic component, has attracted extensive attention due to their unique properties and promising applications in flexible electronics, biosensors, chemical sensors, and neuromorphic systems[4,5]. The stretchable nature of the stretchable OECTs allows them to operate under extreme deformation conditions, making them suitable for wearable and conformal devices that require large deformations. The emergence of this technology not only promotes the innovation of electronic device design, but also offers possibilities for the development of flexible electronics and biosensors. However, current OECTs face the following challenges in practical applications. On one hand, the reported stretchable OECTs show limited transconductance, resulting in relatively low amplification capability and limited electrochemical performances. On the other hand, the reported OECTs that demonstrate high

transconductance often suffer from poor stretchability and low fatigue resistance against stretching. It is a great challenge to achieve OECTs combining both high stretchability and excellent electrical properties such as high transconductance.

Many efforts have been made to enhance the stretchability of OECTs[6-17]. For example, the reported OECT with a folded PDMS substrate can withstand 10% tensile strain and 400 stretch-release cycles[7]. The reported OECT based on a three-dimensional poly(3-hexylthiophene) (P3HT)/styrene-ethylene-butylene-styrene (SEBS) blend porous film exhibits a stretchability of 30% and a peak transconductance ($g_{m,max}$) below 6 mS[8]. Facchetti et al. reported stretchable (30–140% strain) OECTs with a $g_{m,max}$ in the range of 1.5–3 mS based on a semiconducting polymer film with a honeycomb porous microstructure achieved by a pre-stretching method combined with a breath figure tachnique[10]. Besides, stretchable (~30%) OECTs with a $g_{m,max}$ of 22.5 mS based on poly(3,4-ethylenedioxythiophene): poly(styrene sulfonate) (PEDOT:PSS) can be achieved by an inkjet printing method, but the cyclic stability was not mentioned[11]. While there are many

Interdisciplinary Materials Research Center, Department of Polymeric Materials, School of Materials Science and Engineering, Tongji University, Shanghai, PR China. ✉e-mail: yangj@tongji.edu.cn; guoqingzu@tongji.edu.cn; huangjia@tongji.edu.cn

reports on stretchable OECTs, they usually sacrifice the electrical performances such as transconductance. The transconductance of the previously reported state-of-the-art stretchable OECTs is usually lower than 5–20 mS. Therefore, the development of stretchable OECTs with superior electrical properties is urgently needed and represents one of the cutting-edge research areas of OECTs.

In recent years, OECTs based on ionic gel electrolyte are emerging as a promising research direction in the field of transistors due to their superior ionic conductivity, good biocompatibility, and high flexibility of ionic gels[18–26]. The high stretchability of ionic gels can meet the mechanical demands of stretchable OECTs and the three-dimensional network structure of these gels can accommodate a large amount of water and solvent, which can lead to high ion transport efficiency, thus improving the electrochemical performance of OECTs[20]. Furthermore, the use of ionic gel electrolyte not only avoids the leakage issues associated with traditional liquid electrolytes but also improves the stability and usability of the devices[25]. Besides, the interface layers based on ionic gels composed of poly(vinyliflon-hexafluoropropylene) and ionic liquid can improve the ion transport properties of hydrophobic conjugated polymers, which effectively enhances the electrochemical performance of OECTs[27]. The electrochemical performance of OECTs can be enhanced by constructing semiconducting polymer gel active layers with both high ion and charge transport properties. There is one report on rigid OECTs with PEDOT:PSS-based gels as active layers and aqueous solution containing ions as electrolyte. The resulting OECTs exhibit a $g_{m,max}$ of ~40 mS and an on/off ratio of 10^3 [28]. Besides, Lei et al. developed single- and multi-network n-type semiconductor polymer hydrogels with good electron mobility and OECTs based on the hydrogels with a $g_{m,max}$ of ~3 mS[23]. But the reported OECTs based on gel active layers in the above two works are not stretchable. Recently, Wang et al. reported stretchable semiconducting hydrogel-based OECTs with high conformability and immune compatibility[29]. The obtained OECTs exhibit a charge carrier mobility (μ) of 1.4 cm^{-2} V^{-1} s^{-1} and a $g_{m,max}$ of ~4 mS. Inspired by these works, the electrochemical performance of stretchable OECTs may be further enhanced by constructing all-gel OECTs with flexible semiconducting polymer gel and ionic gel as active layer and electrolyte, respectively. However, stretchable all-gel OECTs with gels as both the electrolyte and active layer are rarely reported.

OECTs with good amplification capability show promising applications in pressure sensing[24,30–32] and gas sensing[33–35]. For example, the OECTs with a microstructured gate can regulate the ion transport by changing the contact area between gate and active layer, which can afford pressure sensors with a detection limit of ~10 Pa[31]. Similarly, OECT-based pressure sensors with a detection limit of 1.1 Pa can be obtained by using a pyramid-microstructured gel as the electrolyte layer and a P3HT film as the active layer[32]. The detection limit of the OECT-based pressure sensors may be further decreased by enhancing the transconductance of OECTs and optimizing the structures of the devices. Additionally, OECTs with high transconductance are suitable for highly sensitive gas sensing applications. OECTs with ionic liquids as electrolytes can detect gases such as NH$_3$, NO$_2$, H$_2$S, and SO$_2$ because ionic liquid can adsorb these gases and ion transport will be changed after gas adsorption[33–37]. Stretchable gas sensors show promising applications in wearable electronics and flexible bionic olfactory system. However, highly sensitive stretchable OECT-based gas sensors are rarely reported.

Herein, we report highly stretchable OECTs—all-gel OECTs in which both the active layer and electrolyte are gels. A double-network semiconducting polymer gel consisting of PEDOT:PSS and polyacrylamide (PAM) and a poly(ionic liquid) (PIL) ionogel are used as the active layer and electrolyte of the OECTs, respectively. The flexible network structures of the semiconducting polymer gel active layers and ionogel electrolytes allow the resulting OECTs to reach a good stretchability up to 50%. More importantly, the all-gel network

structures effectively promote ion penetration and transport, which endows the OECTs with a high transconductance of 86.4 mS, on/off ratio of 1.2×10^5, μC_s (C_s is areal capacitance) of 7118.6 μF V^{-1} s^{-1}, and μ of 5.7 cm^{-2} V^{-1} s^{-1}. Benefiting from their unique structures and excellent mechanical/electrical properties, the all-gel OECTs can be used as pressure-sensitive stretchable electronic skins, stretchable artificial synapses, and highly sensitive stretchable olfactory-inspired gas sensors for NH$_3$ detection. This work provides a versatile strategy toward high-performance stretchable all-gel OECTs promising for next-generation high-performance flexible electronics.

Results
Preparation
PEDOT:PSS is a widely used semiconducting polymer with excellent electrochemical properties and high stability. Therefore, PEDOT:PSS is used as one of the semiconductors to prepare semiconducting polymer gel active layer of the all-gel OECTs. Besides, ionic liquid can be used as electrolyte of high-performance OECTs because of its high ionic conductivity and high environmental stability. Hence, PIL ionogel is chosen as the electrolyte of the all-gel OECTs. PEDOT-based gels and PIL ionogels can be obtained via different methods in the literature[38,39]. The PEDOT:PSS/PAM organohydrogel films with a double-network structure were prepared by radical polymerization of the monomer acrylamide (AM) at the presence of a crosslinker and co-assembly of PEDOT:PSS and PAM (Fig. 1a and Supplementary Fig. 1). The PEDOT-based gel film is spin-coated between source and drain electrodes composed of Au and Ag on the polyurethane (PU) substrate to afford an active layer of the OECT. Glycerol was introduced as part of the solvent to ensure the environmental stability of the gel active layer. N,N′-methylenebisacrylamide (MBA) and ammonium persulfate (APS) are used as the crosslinker and thermal initiator in the system, respectively. Semiconducting polymer gels with different PEDOT:PSS contents in the range of 0.21–0.75% were prepared for comparison. PEDOT:PSS is difficult to be dispersed homogeneously when its content is higher than 0.75%. Therefore, the highest PEDOT:PSS content used in this work is 0.75%. To demonstrate the versatility of the all-gel strategy, all-gel OECTs based on p-type poly (2,5-bis (3-triethylene glycol ethoxy thiophene-2-yl)-co-thiophene) (p(g2T-TT)) and n-type poly(benzimidazobenzophenanthroline) (BBL) were also fabricated. The semiconducting polymer gels based on p(g2T-TT) or BBL were prepared by radical polymerization of AM at the presence of p(g2T-TT) or BBL.

The PIL ionogel electrolyte was prepared by radical polymerization of the monomer 1-vinyl-3-butylimidazolium tetrafluoroborate ([VBIm][BF$_4$]) at the presence of a crosslinker (MBA), combined with a spin-coating method (Fig. 1a and Supplementary Fig. 1). Tris (2-hydroxyethyl) methylammonium methylsulfate ([THMA][MeSO$_4$]) is used as the solvent and provides free ions, while 2-hydroxy-4′-(2-hydroxyethoxy)-2-methylpropiophenone (I-2959) is applied as the photoinitiator in the system. All-gel OECT is obtained after the PIL ionogel electrolyte is spin-coated on the gate and semiconducting polymer gel.

The thickness of the semiconducting polymer gel active layer can be adjusted by varying the spin-coating speed in the range of 500–3000 rpm. The thicknesses of the PEDOT:PSS-based gel active layers formed at 500, 1000, 2000, and 3000 rpm are ~267 μm, 4.4 μm, 1.8 μm, and 590 nm, respectively (Supplementary Fig. 2).

Structures and properties of the gels
As shown in the Fourier transform infrared (FTIR) spectra (Supplementary Fig. 3), the peaks of the PEDOT:PSS-based gel at 1448, 1349, and 1650 cm^{-1} are ascribed to the bending of C−H bonds, the stretching of C−C bonds in thiophene ring, and the stretching of C=O bonds, respectively, which are mainly attributed to the presence of PEDOT:PSS and PAM[40,41]. The peaks at 1178, 1008, and 1045 cm^{-1} are

ascribed to the stretching of C–O–C bonds, which are mainly attributed to the presence of PEDOT:PSS[42]. As the content of PEDOT:PSS decreases, the intensity of the peaks corresponding to the stretching of C–O–C bonds gradually becomes weaker.

The chemical structure of the gels is further characterized by X-ray photoelectron spectra (XPS). As shown in Supplementary Fig. 4, the peaks at 531, 399, 284, and 168 eV correspond to O $1s$, N $1s$, C $1s$, and S $2p$, respectively. The S $2p$ peaks of the PEDOT:PSS-based gel at 167.6 and 168.7 eV are ascribed to PSS/APS, while the S $2p$ peaks at 164.6 and 163.4 eV are attributed to PEDOT[43,44]. With the decrease of PEDOT:PSS content, the intensity of the peak corresponding to PEDOT gradually becomes weaker. There is no PEDOT peak observed in the S $2p$ spectrum of the PAM gel without the incorporation of PEDOT. As shown in Supplementary Fig. 5, the O $1s$ peak of the semiconducting polymer gels at 533.2 eV is ascribed to C–O–C bonds and the C $1s$ peak at 286.2 eV is ascribed to C–O/C–S bonds[45], the intensity of which increases with the increase of PEDOT:PSS content in the gels.

Besides, the stretchability of the semiconducting polymer gels and PIL ionogels as well as their electrical properties upon stretching are investigated. The PEDOT:PSS-based gel and PIL iongels can be stretched at least 200% and 400%, respectively, without fracture, indicating the high stretchability of these two kinds of gels (Supplementary Fig. 6 and Supplementary Movies 1–4). They can recover their original shapes after stretching with 100% strain, indicating the high elasticity of the gels (Supplementary Figs. 7, 8 and Movies 5, 6). As shown in Supplementary Figs. 9 and 10, the elongations at break of the PEDOT:PSS-based gel and PIL iongels are 225% and 415%, respectively. Both of the gels can recover nearly their original shapes after stretch-release with 100% strain for 200 cycles, confirming the high stretching stability. The electrical resistance of the gels increases with the increase of tensile strain, and the resistance variation remains relatively stable during stretch-release for 200 cycles. The relative resistance change of the PEDOT:PSS-based gel active layer is ~55% when it is stretched with a large strain of 50%.

The compressibility of these two kinds of gels and their electrical properties upon compression are also studied (Supplementary Figs. 11 and 12). Both of the gels can be compressed 80% without fracture and spring back to their original sizes after they are released,
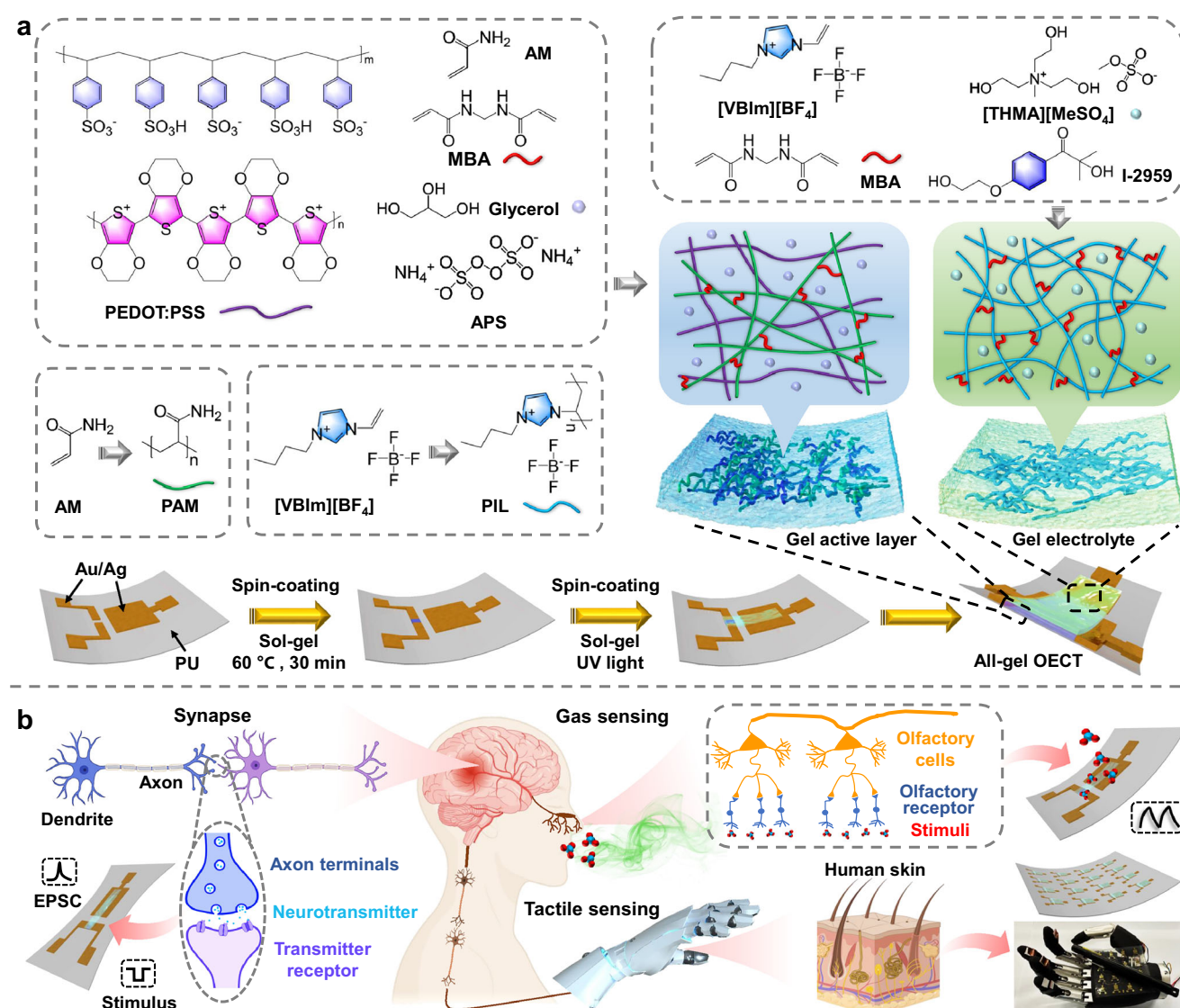

Fig. 1 | Fabrication and applications of all-gel OECTs. a Fabrication of all-gel OECTs. **b** Schematic of applications of all-gel OECTs in tactile sensing, artificial synapses, and gas sensing. Schematic of neuron (left), synapse (left), human body and skin is created in BioRender. Lu, L. (2025) https://BioRender.com/ebbqkgl; https://BioRender.com/s8iepco; https://BioRender.com/r7aljeo.
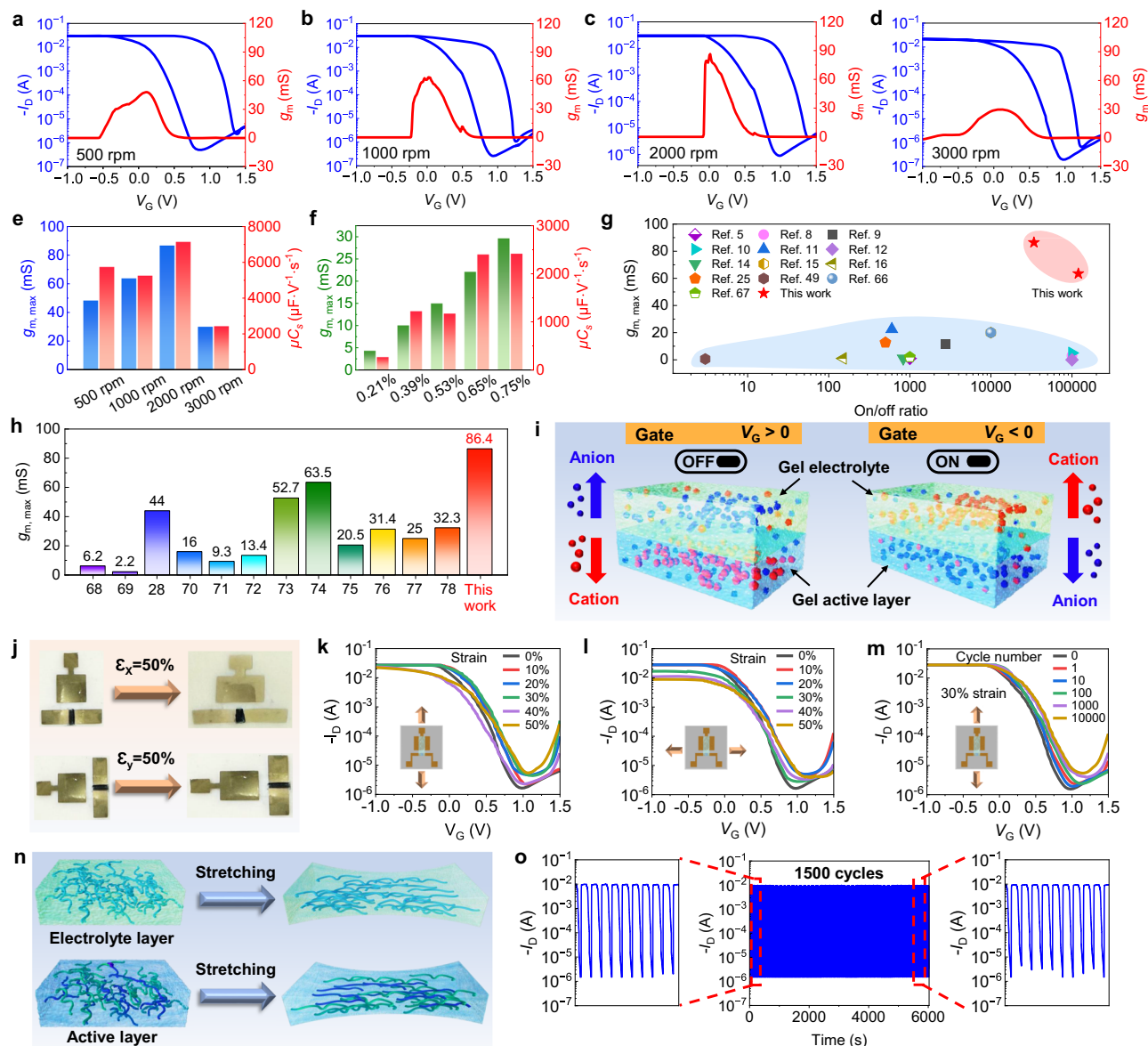
Fig. 2 | Electrical properties of all-gel OECTs based on PEDOT:PSS gel active layer. a–d Transfer and transconductance curves of all-gel OECTs with the gel active layer obtained at different spin-coating speeds. **e** $g_{m, max}$ and μC_s of all-gel OECTs based on gel active layers obtained at different spin-coating speeds. **f** $g_{m, max}$ and μC_s of all-gel OECTs based on gel active layers with different PEDOT:PSS contents under the same spin-coating speed of 3000 rpm. **g** Comparison of $g_{m, max}$ and on/off ratio of our OECTs and the reported stretchable OECTs[5,8–12,14–16,25,49,66,67]. **h** Comparison of $g_{m, max}$ of all-gel OECTs and the reported rigid OECTs based on

PEDOT:PSS[28,68–78]. **i** Illustration of mechanism of ion penetration/transport in gels. **j** Photographs of all-gel OECTs upon stretching along different directions. Transfer curves of all-gel OECTs after stretching along the directions (**k**) perpendicular and (**l**) parallel to channel length with different tensile strains. **m** Transfer curves of all-gel OECTs after stretch-release with 30% strain for different cycles along the direction perpendicular to channel length. **n** Illustration of stretching mechanism of gel active layer and gel electrolyte. **o** Cycling stability of all-gel OECT with 1500 on/off cycles. Source data are provided as a Source Data file.

indicating the high compressibility and elasticity of the gels. They can recover their original shapes after compression-decompression with 50% strain for 200 cycles, indicating the high compression stability. The electrical resistance of the gels decreases with the increase of compressive strain, and the resistance variation is relatively stable during compression-decompression with 50% strain for 200 cycles. The electrical conductivity of the semiconducting polymer gels increases with the increase of PEDOT:PSS contents (Supplementary Fig. 13). The PEDOT:PSS-based gel with a PEDOT:PSS content of 0.75% exhibits a high electrical conductivity of 53 S/cm. The all-gel OECTs based on the semiconducting polymer gels and PIL ionogels are expected to have high stretchability and show potential applications in stretchable pressure-sensitive electronic skins, artificial synapses, and highly sensitive gas sensors (Fig. 1b).

All-gel OECTs

The effects of the semiconducting polymer gel active layer thickness and PEDOT:PSS content on electrical performance of the all-gel OECTs were investigated. As shown in the transfer and transconductance curves of the all-gel OECTs, the $g_{m, max}$ first increases and then decreases with the increase of spin-coating speed (Fig. 2a–d), and the corresponding output curves are presented in Supplementary Fig. 14. The $g_{m, max}$ of the all-gel OECT with a 1.8 μm thick active layer reaches 86.4 mS, higher than those with an active layer thickness of 267 μm (48.0 mS), 4.4 μm (63.5 mS), and 590 nm (29.7 mS) (Fig. 2e). The on/off ratios of the all-gel OECTs with different active layer thicknesses are in the range of 3.4×10^4 to 1.2×10^5, confirming the high on/off ratios. The probable reasons for the increase of transconductance with the decrease of thickness of the active layer in the range of 1.8–267 μm are

shown below. First, for the all-gel OECTs with the active layer thickness larger than 1.8 μm, their drain current probably hardly reaches the saturation state at a relatively fast scanning speed (200 mV s^{-1}) under a fixed duration, which may result in lower transconductance. On the contrary, when its thickness is decreased to 1.8 μm, the active layer of the all-gel OECT will show faster doping speed, which may achieve higher doping level and higher drain current under the same scanning speed and duration, thereby leading to higher transconductance. Second, the percentage of the solvent that evaporates (namely water) during the spin-coating process will become larger when the thickness of the gel active layer becomes smaller. This will result in a relatively larger shrinkage of the gel active layer and the tighter contact among semiconducting polymers inside the gel, which may enhance the values of μ and μC^* (C* is the volumetric capacitance). The detailed reasons are shown in Supplementary Note 1. Besides, because the thickness of the active layers of the all-gel OECTs is larger than those of traditional OECTs (usually smaller than 100 nm), our device show a relatively large voltage hysteresis compared to those of traditional OECTs. The all-gel structure will be further optimized in our future work to reduce the voltage hysteresis.

One of the key figure-of-merit parameters of OECTs is μC^*. The value of μC^* can be calculated from the following equation,

$$g_m = \frac{\mu C^* W d}{L}(V_T - V_G) \tag{1}$$

$$C_s = C^* d \tag{2}$$

where g_m is the transconductance, W is the channel width, L is the channel length, d is the thickness of active layer, V_T is the threshold voltage, C_s is the areal capacitance. The calculated μC_s values of the all-gel OECTs based on PEDOT:PSS gel with active layer thicknesses of 267 μm, 4.4 μm, 1.8 μm, and 590 nm are 5715.5, 5231.5, 7118.6, and 2408.3 μF V^{-1} s^{-1}, respectively (Fig. 2e). It can be seen that the $g_{m, max}$ and μC_s values of the all-gel OECT with an active layer thickness of 1.8 μm are the highest among the fabricated OECTs with different active layer thicknesses. In addition, the effect of different PEDOT:PSS contents on the performance of the all-gel OECTs obtained at a spin-coating speed of 3000 rpm is investigated. It is found that the $g_{m, max}$ and μC_s values of the all-gel OECTs generally increase with the increase of PEDOT:PSS content (Fig. 2f and Supplementary Fig. 15). As a result, the all-gel OECT with the PEDOT:PSS content of 0.75% exhibits higher $g_{m, max}$ and μC_s values compared with those of the OECTs with lower PEDOT:PSS contents.

Furthermore, the areal capacitances of typical PEDOT-based semiconducting polymer gels are measured by an electrochemical impedance spectroscopy method to calculate C_s and μ values (Supplementary Figs. 16 and 17). The calculated C_s of the semiconducting polymer gels with the PEDOT:PSS contents of 0.21%, 0.39%, 0.53%, 0.65%, and 0.75% are 923.4, 2525.4, 2040.8, 1684.8, and 422.5 μF cm^{-2}, respectively. The maximum C_s of the semiconducting polymer gel active layer is among the highest in the reported stretchable PEDOT-based OECTs (Supplementary Table 3). Under a spin-coating speed of 3000 rpm for the gel active layers, the calculated μ value of the all-gel OECT with a 0.75% PEDOT:PSS content is 5.7 cm^2 V^{-1} s^{-1}, which is higher than those of the obtained all-gel OECTs with lower PEDOT:PSS contents (Supplementary Fig. 18). To the best of our knowledge, $g_{m,max}$ (86.4 mS) of the all-gel OECTs is the highest among the previously reported stretchable OECTs (Fig. 2g and Supplementary Table 3). The transconductance of the reported state-of-the-art stretchable OECTs is usually lower than 5–20 mS. The $g_{m,max}$ value is even among the highest in the reported rigid OECTs based on PEDOT:PSS (Fig. 2h). The maximum on/off ratio (1.2 × 10^5) and μ value (5.7 cm^2 V^{-1} s^{-1}) of the all-gel OECTs are also among the highest in the reported stretchable OECTs (Fig. 2g and Supplementary Table 3).

The normalized transconductance ($g_{m,n}$) of OECTs is given by the following equation,

$$g_{m, n} = \frac{g_{m, max}}{d W / L} \tag{3}$$

According to the above equation, the $g_{m,n}$ of the all-gel OECT with a 1.8 μm thick PEDOT:PSS-based gel active layer is calculated to be 24 S cm^{-1}, the value of which is much higher than those of the previously reported OECTs based on semiconducting gels such as PEDOT:PSS hydrogels (~4 S cm^{-1})[28] and p(g2T-T) hydrogels (~2 S cm^{-1})[29].

The all-gel OECT based on p(g2T-TT) gel active layer operates in an accumulation mode (Supplementary Fig. 19). Its $g_{m,max}$ and μC_s reach 53.8 mS and 12373.5 μF V^{-1} s^{-1}, respectively, exceeding those of the previously reported OECTs based on p(g2T-TT) (Supplementary Table 4). After stretching with 30% strain along the direction perpendicular to channel length, no obvious change in transfer and transconductance curves of the p(g2T-TT)-based all-gel OECT are observed and the $g_{m,max}$ retains a high value of 46.6 mS (Supplementary Fig. 19). In addition, the $g_{m,max}$ and μC_s of the all-gel OECT based on BBL gel active layer are 1.3 mS and 245.3 μF V^{-1} s^{-1}, respectively (Supplementary Fig. 20). After stretching with 30% strain along the direction perpendicular to channel length, its peak transconductance still reaches 1.2 mS. The g_m and μC_s of the all-gel OECT based on BBL gel are among the highest in the reported BBL-based OECTs with a similar W/L ratio (Supplementary Table 4).

The high transconductance and on/off ratio of the all-gel OECTs are attributed to the fact that both the active layer and electrolyte are gels. The abundant solvents in the semiconducting polymer gel active layers increase the ion transport paths and the interface area between the semiconducting polymer and the electrolyte, allowing effective ion penetration/transport and efficient doping of the semiconductor (Fig. 2i). The three-dimensional semiconducting polymer network in the gel active layers ensures efficient charge transport along the semiconducting polymer chains.

Besides, since the ionic liquid [THMA][MeSO$_4$] is miscible with water (Supplementary Fig. 21a), ionic liquid in the ionogel electrolyte can diffuse into the semiconducting polymer gel active layer, which can enhance transconductance of OECTs by improving the morphologies of the active layer while maintaining high ion uptake[46–48]. When PAM/NaCl/glycerol/H$_2$O organohydrogel instead of ionogel is used as the electrolyte layer, the measured $g_{m, max}$ and on/off ratio of the all-gel OECT based on PEDOT:PSS gel are 11.0 mS and 2.8 × 10^3, respectively (Supplementary Fig 21c, d), much lower than those of the all-gel OECTs with PIL ionogel as the electrolyte. The transconductance of the OECT based on PEDOT:PSS gel with ionic liquid [THMA][MeSO$_4$] as electrolyte is ~76.2 mS (Supplementary Fig. 22), which is comparable to that of the device by using PIL ionogel as electrolyte (86.4 mS). This further confirms the key role of ionic liquid electrolyte in achieving high transconductance of the PEDOT:PSS-based OECT. Pristine PEDOT:PSS-based gel shows some isolated domains that are probably composed of PEDOT:PSS, which is unfavorable for charge carrier transport (Supplementary Fig. 23)[47,48]. By contrast, no isolated PEDOT:PSS domain is observed and PEDOT:PSS is homogeneously distributed in the skeletons of the PEDOT:PSS-based gel that is treated with ionic liquid (Supplementary Fig. 23). Furthermore, after modification with ionic liquid, the PEDOT:PSS-based gel exhibits larger grains that are probably rich in PEDOT (Supplementary Fig. 24)[47]. These structural characteristics of the PEDOT:PSS-based gel treated with ionic liquid facilitate charge carrier transport. This may contribute to the improved performance of the OECT with PIL ionogel as electrolyte compared to that of the device with PAM/NaCl/glycerol/H$_2$O organohydrogel as electrolyte. Furthermore, the different packing of PEDOT:PSS chains in pristine PEDOT:PSS film and PEDOT:PSS-based gel film is confirmed by grazing-incidence wide-angle X-ray scattering

(GIWAXS) (Supplementary Fig. 25). It should be noted that, PEDOT:PSS cannot be homogeneously dispersed in the ionic liquids [VBIm][BF$_4$] and [THMA][MeSO$_4$], the obtained PEDOT:PSS/[VBIm][BF$_4$]/[THMA][MeSO$_4$] ionogel is inhomogeneous, resulting in the low performance of the OECT with PEDOT:PSS/[VBIm][BF$_4$]/[THMA][MeSO$_4$] ionogel as the active layer and [VBIm][BF$_4$]/[THMA][MeSO$_4$] ionogel as the electrolyte (Supplementary Fig 21b). Therefore, PEDOT:PSS/PAM/glycerol/H$_2$O ionic gel and PIL ionogel are selected as the active layer and electrolyte of the all-gel OECTs, respectively, in this work.

Benefiting from the unique all-gel device structure with highly stretchable gels as both active layer and electrolyte, the all-gel OECT based on PEDOT:PSS gel exhibits high stretchability up to 50% in both directions parallel and perpendicular to channel length (Fig. 2j and Movies 7, 8). When the all-gel OECT is stretched along different directions, the change of transfer curve of the all-gel OECT is relatively small when the tensile strain is within 50% (Fig. 2k, l). The slight current change of the transfer curve of the all-gel OECT is probably attributed to the changes of gel conductivity and W/L values during stretching. The cyclic stretching stability of the all-gel OECT is tested by stretch-release with 30% strain in the direction perpendicular to channel length for 10,000 cycles. The transfer curves of the all-gel OECT are relatively stable after stretch-release with 30% strain for 10,000 cycles, indicating the high stretching stability of the all-gel OECTs (Fig. 2m).

There are several reasons for the high stretchability of the all-gel OECT. First, the semiconducting polymer gel active layer and PIL ionogel electrolyte exhibit high stretchability and elasticity (Supplementary Figs. 6–10). The deformation and orientation (along the stretching direction) of the disordered and crimpled macromolecular chains in the gels can endure large tensile strains, leading to high stretchability, while the crosslinked 3D network structure endows the gels with high elasticity (Fig. 2n). Second, the relative resistance change of the semiconducting polymer gel and PIL ionogel is relatively small (50–55%) when they are stretched with a large strain of 50% (Supplementary Figs. 9 and 10). There will be fewer amount of contact points between PEDOT chains during stretching with 0–50% tensile strain, resulting in an increase in resistance of the semiconducting polymer gel (Fig. 2n). Third, the PU substrate exhibits high stretchability. Fourth, the Ag/Au electrodes (source, drain, and gate) on the PU substrate are highly stretchable[49,50]. The optical microscope image shows that there is no obvious crack on the surface of the Ag/Au electrode as the all-gel OECT is stretched by 0–50% (Supplementary Fig. 26). The resistance of the Ag/Au electrode remains small (19.5 Ω) at a large tensile strain of 50%.

Furthermore, the on/off cycling stability of the all-gel OECT is investigated by switching gate voltage between −0.5 V and 1.0 V under a fixed drain voltage of −0.5 V. The drain current of the all-gel OECT based on PEDOT:PSS gel exhibits negligible degradation after 1500 on/off cycles, indicating the high on/off cycling stability of the all-gel OECT (Fig. 2o). Besides, the transfer curve of the all-gel OECT remains nearly unchanged after 10 days, indicating the good environmental stability of the device (Supplementary Fig. 27).

Pressure-sensitive electronic skin

Because of the high transconductance and stretchability of the all-gel OECTs consisting of highly compressible and elastic ionogel electrolyte and semiconducting polymer gel active layer, they can be applied as highly sensitive stretchable pressure sensors promising for electronic skins, artificial intelligence, and robots[24,30–32,51,52]. The all-gel OECT based on PEDOT:PSS gel with an active layer thickness of 1.8 μm and PEDOT:PSS content of 0.75% is used to investigate the pressure sensing performance. To improve the sensitivity of pressure sensing, a pyramid-shaped microstructured surface of the ionogel electrolyte layer is constructed (Fig. 3a, b). The width × length × height of the pyramid-shaped microstructure is 500 × 500 × 1000 μm, while the distance between each pyramid microstructure is 300 μm

(Supplementary Fig. 28). For the pressure sensors with a vertical gate structure, the microstructured surface faces the gate (Fig. 3a, b), while for those with a coplanar gate structure, the microstructured surface faces both the gate and active layer (Fig. 3c, d).

In the case of the all-gel OECT pressure sensor with a vertical gate structure, the drain current changes significantly in response to different pressures, indicating the capability of detecting pressure stimuli (Fig. 3e). At a constant V_G of −0.5 V, the drain current (I_D) increases with the increase of applied pressure (Fig. 3f), while when $V_G = 0.5$ V, I_D decreases with the increase of applied pressure (Supplementary Fig. 29). An obvious current response of the all-gel OECT pressure sensor can be recorded in real time under an external pressure stimulus (Fig. 3g). It should be noted that the response of the OECT pressure sensor to different pressures is relatively stable when it is stretched 30% along the direction perpendicular to channel length, indicating the good stretching stability of the device (Fig. 3h). In the case of the all-gel OECT pressure sensor with a coplanar gate structure, the I_D change tendency under external pressures is similar to that of the pressure sensor with a vertical gate structure (Fig. 3i).

The working mechanism of the all-gel OECT pressure sensor is based on the intercalation and de-intercalation of ions in the conjugated polymer active layer (electrochemical doping/de-doping of the semiconductor) modulated by external pressures[24,30–32]. According to the Bernards model, OECT can be divided into an electronic circuit and an ionic circuit, where the ionic circuit is composed of a gate/electrolyte capacitor (C_G), electrolyte resistor (R_E), and electrolyte/channel capacitor (C_{CH}) (Fig. 3a)[24,30–32]. In the case of the OECT with a vertical gate structure, the gate voltage mainly drops at the gate-electrolyte interface in the absence of external pressure because the contact area between the gate and electrolyte with a microstructured surface is small and the resulting C_G is small. Consequently, the gate voltage drop at the electrolyte-channel interface is small and the injection of electrolyte anions into the channel is limited when a negative gate voltage is applied, resulting in a relatively low drain current. Under the applied pressure, the height of the pyramid structure becomes smaller and the contact area between gate and electrolyte increases, which increases C_G and reduces the gate voltage drop at the gate-electrolyte interface, thus enhancing the gate voltage drop at the electrolyte-channel interface. In this case, more electrolyte anions ([BF$_4$]$^-$ and [MeSO$_4$]$^-$) are injected into the channel under a negative gate voltage, resulting in the electrochemical doping of the active layer with a larger number of holes, thereby enhancing the drain current of the OECT (Fig. 3j)[32,53]. In addition, the finite element analysis (FEA) mechanical simulation was carried out to investigate the structure variation and stress/strain distribution of the PIL ionogel electrolyte layer with a pyramid-shaped microstructured surface (Supplementary Figs. 30, 31, and Movies 9, 10). Under external pressures, the pyramid-shaped microstructure is deformed and its height is decreased. The microstructure becomes flattened when the compressive strain reaches 80%. The above FEA simulation is consistent with the experimental results. Benefiting from the high transconductance of the OECT and the microstructured surface of the PIL ionogel electrolyte, the all-gel OECT pressure sensor exhibits a low detection limit of 0.1 Pa, the value of which is the lowest among the previously reported OECT pressure sensors (Fig. 3k and Supplementary Table 5).

In order to explore potential application of the all-gel OECT pressure sensors in the field of electronic skin, a 4 × 4 all-gel OECT pressure sensor array on a PU film was fabricated (Fig. 3l). The electronic skin based on the all-gel OECT pressure sensor array has excellent stretchability and bendability (Fig. 3m and Supplementary Fig. 32). The signal output of the sensor array fixed on the palm of a bionic hand is consistent with the position and shape of a pen placed on the palm (Fig. 3n). When the bionic hand grasps an apple and an egg, the pressure distribution on the palm is accurately detected (Fig. 3o and Supplementary Fig. 33). Evidently, the all-gel OECT
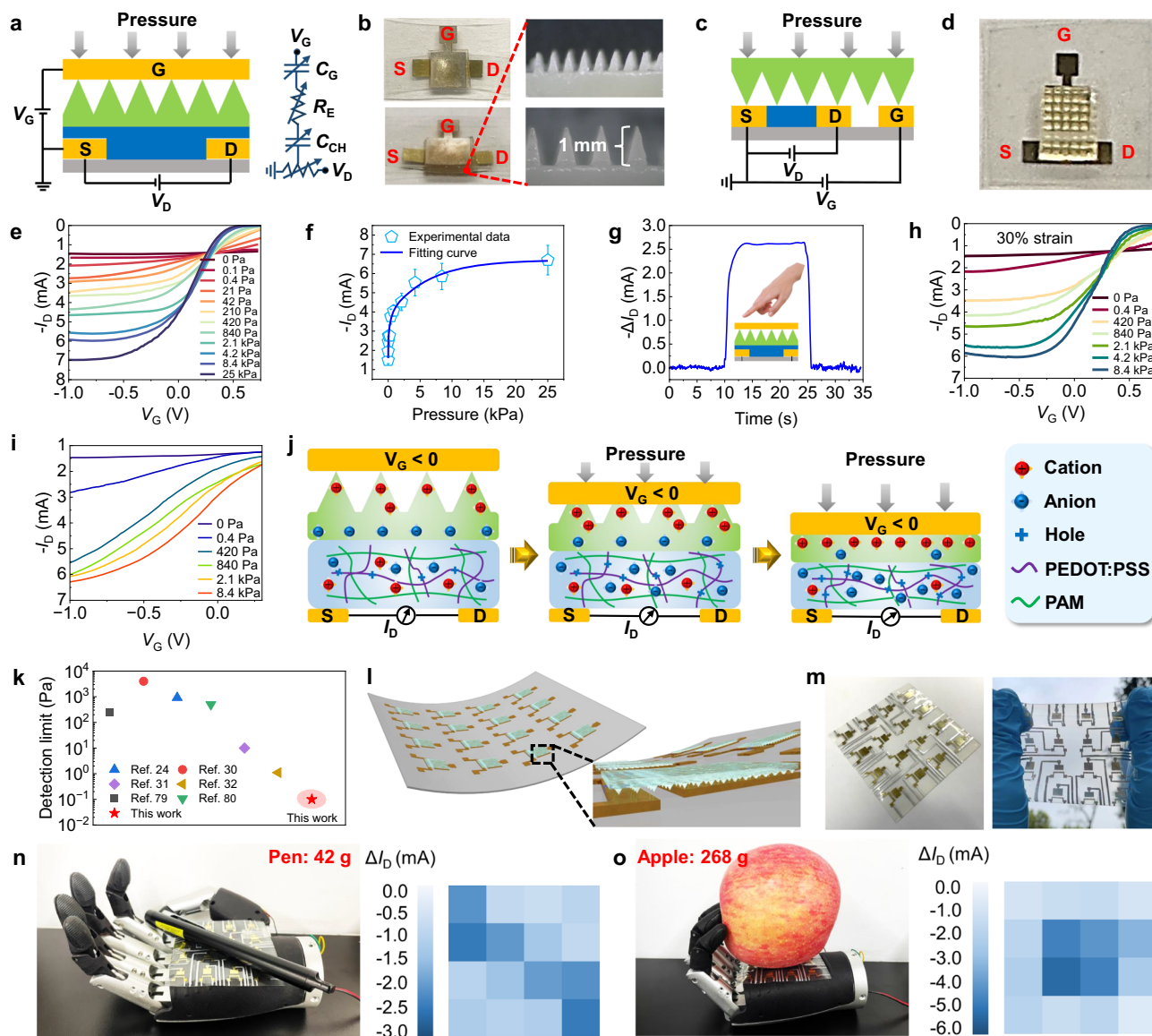
Fig. 3 | Stretchable pressure-sensitive electronic skin based on all-gel OECTs.
a Structure diagram and **b** photographs of all-gel OECT pressure sensor with a
vertical gate structure. **c** Structure diagram and **d** photographs of all-gel OECT
pressure sensor with a coplanar gate structure. **e** Transfer curves and **f** I_D
($V_G = -0.5$ V) of all-gel OECT pressure sensor with a vertical gate structure under
different pressures. **g** Response of all-gel OECT pressure sensor under an external
pressure stimulus (pressed by a finger) at the V_G of −0.5 V. **h** Transfer curves of the
stretched all-gel OECT pressure sensor with 30% strain along the direction per-
pendicular to channel length under different pressures. **i** Transfer curves of all-gel

OECT pressure sensor with a coplanar gate structure under different pressures.
j Sensing mechanism diagram of all-gel OECT pressure sensor. **k** Comparison of
pressure detection limit of our OECT pressure sensor and the previously reported
OECT pressure sensors[24,30–32,79,80]. **l** Structure diagram and **m** photographs of a 4 × 4
all-gel OECT pressure sensor array. **n**, **o** Tactile perception of all-gel OECT-based
electronic skin fixed on a bionic hand. Error bars represent the standard deviation
from at least three independent measurements. Source data are provided as a
Source Data file.

pressure sensor array shows promising applications in pressure-
sensitive electronic skins of robots, bionic hands, and prostheses.

Artificial synapse

Another important application of OECTs is artificial synapses for
neuromorphic simulation[54–56]. The all-gel OECTs can be used as
stretchable artificial synapses to simulate biological synaptic beha-
viors. The biological synapse is composed of presynaptic membrane,
synaptic cleft, and postsynaptic membrane, and is located between
presynaptic and postsynaptic neurons. The axonal terminals can
release neurotransmitters that pass through the synaptic cleft to
dendrites, allowing the synapse able to transmit signals. Here, V_G pulse
and I_D are used to simulate presynaptic pulse and excitatory post-
synaptic current (EPSC), respectively (Fig. 4a). When a presynaptic V_G

pulse with a width of 100 ms triggers the synaptic all-gel OECT based
on PEDOT:PSS gel, I_D increases quickly to a maximum value and then
gradually decreases, showing the EPSC characteristic (Fig. 4b). When
the all-gel synaptic OECT is stretched by 30% along the direction
perpendicular to channel length, the EPSC remains nearly unchanged,
indicating the high stretching stability of the artificial synapse (Fig. 4b).

Besides, the all-gel OECT can simulate pair-pulse facilitation (PPF)
behavior by applying two consecutive presynaptic pulses[57]. When two
consecutive V_G pulses with the same width (100 ms) are applied, I_D of
the all-gel synaptic OECT triggered by the second pulse is larger than
that triggered by the first pulse (Fig. 4c). This phenomenon is con-
sistent with the characteristic of PPF behavior. The PPF behavior of the
all-gel synaptic OECT remains nearly unchanged when it is stretched
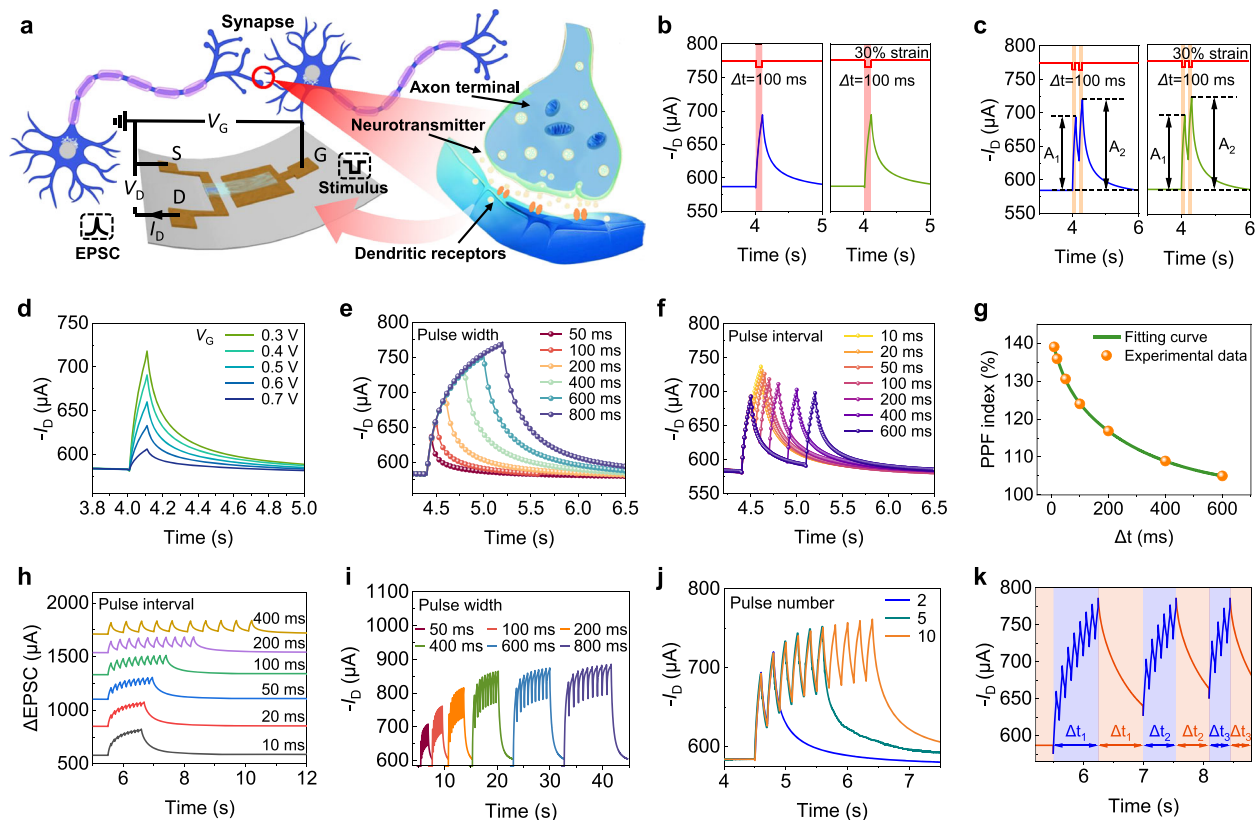30% along the direction perpendicular to channel length, further

Fig. 4 | Stretchable all-gel OECT artificial synapses based on PEDOT:PSS gel active layer. a Mechanism diagram of all-gel synaptic OECT. Schematic of neuron is created in BioRender. Lu, L. (2025) https://BioRender.com/9pwzn0x. EPSC of all-gel OECT before and after stretching with 30% strain triggered by **b** one and **c** two V_G pulses ($V_G = 0.4\,V$). EPSC of all-gel OECT triggered by one V_G pulse with **d** various V_G values and **e** pulse widths ($V_G = 0.5\,V$). **f** EPSC of all-gel OECT triggered by two V_G pulses with various pulse intervals. **g** PPF index of all-gel OECT under various pulse intervals. EPSC of all-gel OECT triggered by ten V_G pulses with **h** various pulse intervals and **i** pulse widths. **j** EPSC of all-gel OECT triggered by consecutive V_G pulses with different pulse numbers under the same pulse width (100 ms). **k** Simulation of learning-forgetting-relearning process by all-gel synaptic OECT with a pulse width of 50 ms and a pulse interval of 50 ms. Source data are provided as a Source Data file.

confirming its high stretching stability (Fig. 4c). When the V_G value of the V_G pulse baseline is 0.8 V, the EPSC decreases with increasing the V_G value in the range of 0.3–0.7 V (Fig. 4d) and increases with increasing the V_G pulse width in the range of 50–800 ms (Fig. 4e). The maximum current value of the second postsynaptic pulse decreases with the increase of V_G pulse interval in the range of 10–600 ms, which indicates that the V_G pulse interval has significant influence on PPF behavior (Fig. 4f). PPF index is given by the equation: PPF index = A_2/$A_1 \times 100\%$, where A_1 and A_2 are the maximum ΔEPSC triggered by the first and second V_G pulse, respectively. As the V_G pulse interval increases, the PPF index decreases significantly (Fig. 4g). When ten consecutive V_G pulses are applied to the all-gel synaptic OECT, ΔEPSC tends to become larger with the decrease of pulse interval (Fig. 4h). The change of EPSC tends to become saturated when the V_G pulse width and V_G pulse number increases (Fig. 4i, j).

When human learn new knowledge, the brain goes through three processes: learning, forgetting, and relearning. The relearning process takes less time compared to that of the initial learning process[58–60]. Because of the above synaptic characteristic, the all-gel synaptic OECTs have the ability to simulate the learning-forgetting-relearning process. The learning-forgetting-relearning process can be simulated by applying V_G pulses with different pulse numbers (Fig. 4k). The first learning process is simulated by applying 8 consecutive V_G pulses to trigger the postsynaptic pulses. The first forgetting process is simulated by the decrease of EPSC after removing the V_G pulse. Then, the previous learning level can be achieved by applying only 6 consecutive V_G pulses. After another forgetting process, only 4 V_G pulses are

needed to recover the previous learning level. As we can see, the all-gel synaptic OECTs show promising applications in stretchable artificial synapses and neuromorphic simulations.

Gas sensor

The olfactory system is one of the six basic human sensory nervous systems. After binding with odor molecules, olfactory receptor proteins activate olfactory receptor cells and trigger the transmission of neural signals. These signals are converted into electrical signals, which are transmitted to the brain's olfactory bulb through the olfactory nerve. In the olfactory bulb, neural signals are further integrated, decoded, and analyzed to produce odor perception and discrimination[61]. Because of the gas sensing capability and the dynamic ion-to-electron transduction that is similar to the characteristic of biological synapse, the all-gel OECTs can be used to simulate the human olfactory system to perceive toxic and harmful gases in the environment and avoid harm to the human body (Fig. 5a). NH_3 is a kind of colorless and irritating alkaline gas. After NH_3 is inhaled into the lung, it is easy to enter the blood through the alveoli and bind to hemoglobin, thus destroying the oxygen transport function of oxygen. When the concentration of NH_3 in the air reaches a certain level ($>0.1\,mg/m^3$), it will cause harm to the human body[57]. Therefore, the development of all-gel OECT gas sensor for detecting the leakage of NH_3 is beneficial for protecting environment and human health.

NH_3 molecules can be adsorbed by the PIL ionogel electrolyte and the free ionic liquid in the ionogel is able to combine with NH_3[33]. Under the positive gate voltage (0.5 V), the [THMA]$^+$ cations and NH_3
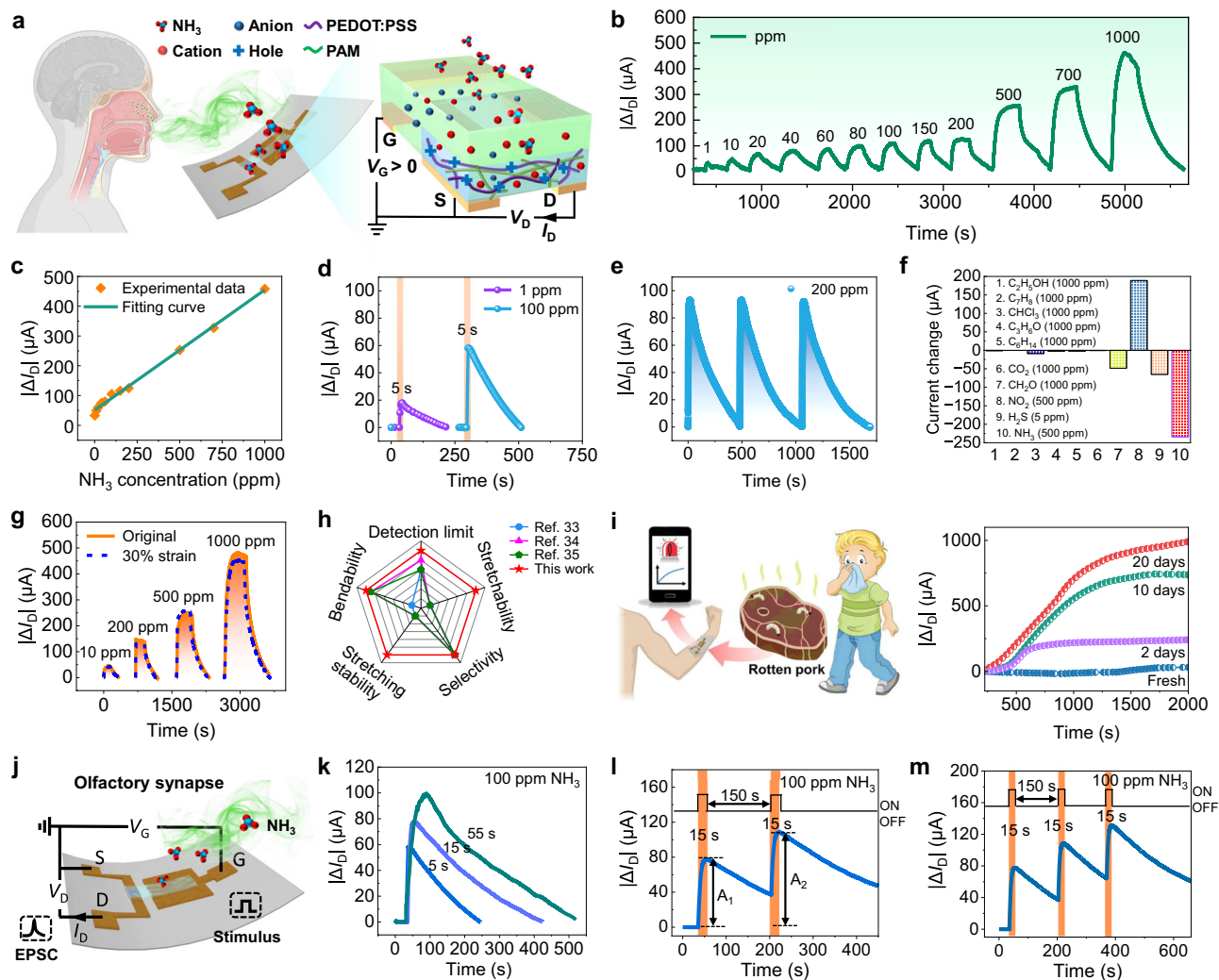
Fig. 5 | Stretchable all-gel OECT gas sensors based on PEDOT:PSS gel active layer. **a** Mechanism diagram of gas sensing of all-gel OECT. Schematic of human body is created in BioRender. Lu, L. (2025) https://BioRender.com/8l76b8o. **b** The continuous response of all-gel OECT to NH_3 with different concentrations. **c** Response of all-gel OECT versus NH_3 concentration. **d** Response of all-gel OECT upon exposure to 1 and 100 ppm NH_3 for the same duration time of 5 s. **e** Response of all-gel OECT to 200 ppm NH_3. **f** Selectivity of all-gel OECT gas sensor. **g** Response of all-gel OECT to different concentrations of NH_3 before and after stretching with 30% strain. **h** Comparison of detection limit, stretchability, selectivity, stretching stability, and bendability of our OECT gas sensor and the previously reported OECT gas sensors[33-35]. **i** Response of all-gel OECT to rotten pork. **j** Schematic illustration of olfactory synapse based on all-gel OECT. **k** Drain current change induced by 100 ppm NH_3 pulse with different pulse duration. **l** PPF behavior induced by a pair of 100 ppm NH_3 pulses with a pulse width of 15 s and a pulse interval of 150 s. **m** Drain current change induced by 3 consecutive 100 ppm NH_3 pulses. Source data are provided as a Source Data file.

combined with the ions in the ionogel can be injected into the semi-conducting polymer gel active layer. The p-type hole-conducting PEDOT will be doped by the electron-rich NH_3 that acts as an electron donor, which reduces the carrier density of the active layer, thus decreasing the drain current[33]. The continuous response of the all-gel OECT gas sensor exposed to different concentrations of NH_3 is examined. The drain current decreases and $|\Delta I_D|$ increases with the increase of the concentration of NH_3 (Fig. 5b). The detection limit of the all-gel OECT gas sensor to NH_3 is as low as 1 ppm. The sensor exhibits a relatively long recovery time because the adsorption and desorption of NH_3 in the ionogel electrolyte and semiconducting polymer gel active layer are relatively slow processes[62,63]. The response of the all-gel OECT versus NH_3 concentration and the corresponding fitting curve are shown in Fig. 5c. Under the exposure to 1 and 100 ppm NH_3 for the same duration time of 5 s, the drain current decrements of the all-gel OECT are 18 and 65 μA, respectively (Fig. 5d). When the all-gel OECT is exposed to 200 ppm NH_3 for three times in succession, the response of the all-gel OECT is nearly unchanged, confirming the good stability of the all-gel OECT gas sensor for NH_3 detection (Fig. 5e).

To evaluate the selectivity of the all-gel OECT gas sensor for NH_3 detection, the response of the sensor to potential interfering gases (1000 ppm ethanol (C_2H_5OH), 1000 ppm toluene (C_7H_8), 1000 ppm trichloromethane ($CHCl_3$), 1000 ppm acetone (C_3H_6O), 1000 ppm hexane (C_6H_{14}), 1000 ppm carbon dioxide (CO_2), 1000 ppm for-maldehyde (CH_2O), 500 ppm nitrogen dioxide (NO_2), and 5 ppm hydrogen sulfide (H_2S)) are also tested. The current change tendency of the all-gel OECT gas sensor in response to NO_2 is opposite to that of the device in response to H_2S and NH_3. Although the device shows response to H_2S and NO_2, its response to 500 ppm NH_3 is higher than those of other gases such as 500 ppm NO_2 (Fig. 5f). The different responses of the device to various gases are probably attributed to the different solubility of the gases in the electrolyte and different inter-actions of the electrolyte and PEDOT with various gases[64]. In addition, the stretchability of the all-gel OECT gas sensor is investigated. It is found that there is almost no difference in response of the sensor to the same concentration of NH_3 before and after stretching with 30% strain along the direction perpendicular to channel length, indicating the good stretchability of the all-gel OECT gas sensor (Fig. 5g). As we

can see, the all-gel OECT gas sensor proposed in this work exhibits an excellent combination of low detection limit, good stretchability, high selectivity, good stretching stability, and bendability (Supplementary Fig. 34), which is difficult to be achieved by traditional OECT-based gas sensors (Fig. 5h and Supplementary Table 6). These properties make the all-gel OECT gas sensor able to be used as wearable electronics that require large deformations.

Because of its high sensitivity, the all-gel OECT gas sensor is suitable for food quality monitoring and toxic gas warning. In many household refrigerators and placement area of ingredients in public restaurants, it is difficult to tell whether food, especially meat, is rotten only by smell and the naked eye alone. In the process of meat spoilage, protein decomposition will produce a variety of intermediate or final gas products, including NH_3, hydrogen sulfide, and carbon dioxide[65]. The all-gel OECT can be used to detect NH_3 produced by rotting meat in a sealed box (Fig. 5i and Supplementary Fig. 35). The sensor has no response to fresh pork. However, after 2–20 days, the all-gel OECT exhibits obvious drain current changes. It can be seen that the all-gel OECT gas sensor has the capability of detecting toxic gases and monitoring food quality in real time.

Furthermore, the all-gel OECTs can be applied as artificial olfactory synapses (Fig. 5j). The relatively long recovery time of the all-gel OECT gas sensor demonstrates the memory storage characteristic. The transition from short-term memory (STM) to long-term memory (LTM) can be achieved by the all-gel OECT gas sensor with prolonged exposure to NH_3 (Fig. 5k). In addition, the all-gel OECT can simulate PPF behavior by applying two consecutive gas pulses (Fig. 5l). The $|\Delta I_D|$ value triggered by the second gas pulse is higher than that of the first one, indicating that synaptic weight can be enhanced by applying successive gas pulses. The maximum $|\Delta I_D|$ value can be further enhanced by applying more NH_3 pulses (Fig. 5m). These characteristics make the all-gel OECTs able to memorize the accumulated exposure to toxic gases, further confirming the capability of the all-gel OECTs to simulate olfactory perception process of humans.

In practical applications, the all-gel OECT pressure sensor can be sealed by a polydimethylsiloxane (PDMS) or PU film to prevent the interference induced by gas molecules. In the case of the all-gel OECT gas sensor, the gel electrolyte does not have a microstructured surface. The micostructured surface of the gel electrolyte is crucial for achieving highly sensitive pressure sensing. The gas sensor without a microstructured surface shows negligible response to external pressure. Besides, all-gel OECTs are advantageous for further integration, which will be done in our future works.

The major importance of this work are summarized as follows. (1) Highly stretchable OECTs−all-gel OECTs with gels as both electrolyte and active layer− have been developed. (2) The all-gel network structure based on ionogel electrolyte and semiconducting polymer gel active layer promotes deeper ion penetration and efficient doping of semiconductor. (3) The all-gel OECTs combine ultra-high transconductance (86.4 mS), high on/off ratio (1.2×10^5), and good stretchability (50%), which achieves an excellent balance between stretchability and electrical properties of OECTs. (4) The transconductance of the all-gel OECTs is ~4–10 times higher than those of state-of-the-art stretchable OECTs. (5) The stretchable all-gel OECT-based pressure sensors exhibit a detection limit of 0.1 Pa, which is lower than those of the previously reported OECT pressure sensors. (6) The all-gel OECT gas sensor combines low detection limit, high selectivity, and good stretchability, which is a combination not observed with traditional OECT gas sensors.

The all-gel strategy proposed in this work is versatile and can be used to develop various high-performance stretchable OECTs and ion-gated transistors. In our further works, all-gel OECTs with different structures and semiconductors will be investigated. Besides, other properties such as biosensing performance will be explored to broaden their applications.

Discussion

In summary, we have developed high-performance and stretchable all-gel OECTs utilizing PIL ionogels as electrolytes and semiconducting polymer gels as active layers. The all-gel structure of electrolyte and active layer of OECTs effectively promotes ion penetration and transport, enabling efficient doping of the semiconductor, while the flexible gel electrolyte and active layer endows the all-gel OECT with good stretchability. The all-gel OECTs combine high transconductance of 86.4 mS, on/off ratio of 1.2×10^5, μC_s of 7118.6 $\mu F\ V^{-1}\ s^{-1}$, μ of 5.7 $cm^{-2}\ V^{-1}\ s^{-1}$, stretchability up to 50%, and excellent stretching stability (10,000 cycles under 30% strain). The resulting all-gel OECT pressure-sensitive electronic skins combine a good stretchability and a low detection limit of 0.1 Pa. Furthermore, the all-gel OECTs can be applied as stretchable artificial synapses capable of emulating biological synaptic behaviors such as EPSC, PPF, and learning-forgetting-relearning process. Additionally, the all-gel OECTs can simulate the perception process of human olfactory system, making them high-performance gas sensors combining low detection limit, high selectivity, good stretching stability, and the capability of food quality monitoring. This work provides an idea for the design of high-performance stretchable transistors promising for flexible electronics, sensors, logic circuits, healthcare, human-machine interfaces, etc.

Methods
Materials
Poly(3,4-ethylenedioxythiophene): poly(styrene sulfonate) (PEDOT:PSS, PH1000) was supplied by Heraeus Deutschland GmbH & Co. KG. Acrylamide (AM), glycerol, APS, MBA, 1-vinyl-3-butylimidazolium tetrafluoroborate ([VBIm][BF$_4$]), tris (2-hydroxyethyl) methylammonium methylsulfate ([THMA][MeSO$_4$]), 2-hydroxy-4′-(2-hydroxyethoxy)-2-methylpropiophenone (I-2959), and N,N-dimethylformamide (DMF) were supplied by Shanghai Aladdin Biochemical Technology Co., Ltd. Polyurethane (PU) particles were provided by Suzhou Kunsheng Biodegradable New Material Co., Ltd. NH_3 was purchased from Jiangsu Xinyiyang Chemical Co., Ltd. Sodium chloride (NaCl), ethanol, toluene, trichloromethane, acetone, hexane, mineral oil, dimethylsulfoxide (DMSO), methane sulfonic acid (MSA), and formaldehyde were supplied by Shanghai Titan Scientific Co., Ltd. Poly (2,5-bis (3-triethylene glycol ethoxy thiophene-2-yl)-co-thiophene) (p(g2T-TT)) and n-type poly(-benzimidazobenzophenanthroline) (BBL) were purchased from Aode Microelectronics Technology Co., Ltd. Carbon dioxide, nitrogen dioxide, and hydrogen sulfide were provided by Shanghai Weichuang Standard Gas Analysis Technology Co., Ltd. All the chemicals were used as received.

Preparation of PEDOT:PSS-based gels
AM, deionized water, and glycerol were mixed with a mass ratio of 1:3:3. The PEDOT:PSS dispersion (13 mg/mL) was concentrated to a PEDOT:PSS dispersion with a concentration of 20 mg/mL by heating and evaporation in an oven at 60 °C. AM/deionized water/glycerol solution (0.8 g) and 0.5 g concentrated PEDOT:PSS dispersion (20 mg/mL) were then mixed completely with stirring, followed by the addition of 0.0125 g MBA and 0.01 g APS. After radical co-polymerization of AM and MBA at 60 °C for 30 min, double-network semiconducting polymer gels composed of PEDOT:PSS and PAM with a PEDOT:PSS content of 0.75% were obtained. Besides, the semiconducting polymer gels with different PEDOT:PSS contents (0.21%, 0.39%, 0.53%, and 0.65%) were also prepared for comparison.

Preparation of p(g2T-TT)-based gels
The p(g2T-TT)-based gel was prepared via the following method. p(g2T-TT) was dispersed in DMSO to obtain a p(g2T-TT) dispersion (10 mg mL^{-1}), while AM was dissolved in DMSO to afford an AM solution (25 wt%). Subsequently, the p(g2T-TT) dispersion (0.5 g) was mixed with 0.8 g AM solution, followed by adding 0.0125 g MBA and

0.01 g APS. The mixed dispersion was spin-coated on a substrate. After heat treatment at 60 °C for 30 min, gel was formed. The solvent of the gel was exchanged with [THMA][MeSO$_4$] to afford a p(g2T-TT)-based gel film.

Preparation of BBL-based gels

The BBL-based gel was prepared by the following method. BBL was dispersed in MSA to obtain a BBL dispersion (10 mg mL^{-1}), while AM was dissolved in MSA to afford an AM solution (23 wt%). Subsequently, the BBL dispersion (0.5 g) was mixed with 1.28 g AM solution, followed by adding 0.0125 g MBA and 0.01 g APS. The mixed dispersion was spin-coated on a substrate. After heat treatment at 60 °C for 30 min, gel was formed. The gel was subjected to solvent exchange with water and [THMA][MeSO$_4$] to afford a BBL-based gel film.

Preparation of PIL ionogels

Ionic liquid monomer [VBIm][BF$_4$] (1.8 g), 0.9 g ionic liquid [THMA][MeSO$_4$], 0.0018 g crosslinker MBA, and 0.0036 g photoinitiator I-2959 were mixed completely with stirring. After radical co-polymerization of [VBIm][BF$_4$] and MBA under ultra-violet (UV) light irradiation, PIL ionogels were obtained.

Fabrication of stretchable all-gel OECTs

PU particles were dissolved by DMF and coated on a glass slide followed by drying at 60 °C and peeling off the glass slide to afford a stretchable PU film as the substrate of the OECTs. 30-nm-thick Ag and 15-nm-thick Au were deposited on the PU film as the source, drain, and gate of the OECTs with a coplanar gate structure by thermal evaporation using a shadow mask. The channel width (W) and length (L) were 2000 and 100 μm, respectively, leading to a W/L value of 20.

Subsequently, semiconducting polymer gel active layers were prepared. The semiconducting polymer-based mixed dispersion (-0.5 μL) composed of semiconducting polymer (PEDOT:PSS, p(g2T-TT), or BBL), AM, MBA, solvent, and APS was dropped on the channel between source and drain, followed by spin-coating. It was then heated at 60 °C for 30 min to form the semiconducting polymer gel film. In the case of the gel based on p(g2T-TT) or BBL, its solvent was exchanged with [THMA][MeSO$_4$]. In order to obtain reliable experimental results on electrical properties, the gel active layers of the all-gel OECTs were patterned by scrapping off unnecessary gels. The unnecessary gel was scraped off using a small cotton swab to obtain a desired shape of the gel active layer. The spin-coating speeds were 500, 1000, 2000, and 3000 rpm for PEDOT:PSS-based gel, while it was kept at 2000 rpm for the gel based on p(g2T-TT) or BBL. For all the semiconducting polymer gel, the spin-coating time was kept at 15 s.

The ionic liquid solution (-2 μL) composed of [VBIm][BF$_4$], [THMA][MeSO$_4$], MBA, and I-2959 was spin-coated on the top of the semiconducting polymer gel active layer and the gate electrode. The spin-coating speed was 1000 rpm and the spin-coating time was 15 s. After the formation of PIL ionogel electrolyte under UV light irradiation, the excess part of the gels was erased to obtain the desired shape of the gel electrolyte to afford stretchable all-gel OECTs. Both the gel active layer and electrolyte had a roughly rectangular shape. For all the all-gel OECT devices, the width × length of the gel active layer and electrolyte was -0.8 mm × 2 mm and 3 mm × 6 mm, respectively.

Fabrication of pressure-sensitive electronic skin

The all-gel OECT with an active layer thickness of 1.8 μm and PEDOT:PSS content of 0.75% was used to fabricate the OECT pressure sensors. The shape and size of the gate, source, and drain of the OECT pressure sensor with a vertical gate structure were shown in Supplementary Fig. 36. The fabrication process of the gate electrode of the OECT pressure sensors was shown below. The stretchable PU substrates were prepared via the aforementioned method. A Ag/Au thin film with a desired shape (Supplementary Fig. 36a) was deposited on

the PU substrate via thermal evaporation using a vacuum evaporation equipment. Specifically, the 30-nm-thick Ag was deposited on the PU substrate by thermal evaporation using a customized shadow mask with the desired shape, followed by the deposition of 15-nm-thick Au via the same thermal evaporation method using the same shadow mask. The obtained 30-nm-thick Ag/15-nm-thick Au thin film was used as the gate of the OECTs with a vertical gate structure. Similarly, 30-nm-thick Ag and 15-nm-thick Au were deposited on another PU film by thermal evaporation using a different shadow mask to serve as the source and drain of the OECT pressure sensors (Supplementary Fig. 36b). A PIL ionogel with a pyramid-shaped microstructured surface was used as the electrolyte. The ionic liquid solution composed of [VBIm][BF$_4$], [THMA][MeSO$_4$], MBA, and I-2959 was poured into a microstructured template made of PDMS and crosslinked under UV light irradiation to form an ionogel with a quadrangular pyramid microstructure. The width × length × height of the pyramid-shaped microstructure was 500 × 500 × 1000 μm, and the distance between each microstructure was 300 μm. For the pressure sensors with a vertical gate structure, the ionogel electrolyte was sandwiched between the gate and semiconducting polymer gel active layer and the microstructured surface faced the gate. For the pressure sensors with a coplanar gate structure, the ionogel electrolyte was put on the surface of the gate and semiconducting polymer gel active layer with the microstructured surface facing both the gate and active layer.

For the fabrication of the electronic skin based on an all-gel OECT pressure sensor array, a 4 × 4 Ag/Au source/drain/gate electrodes array were deposited on PU substrate via thermal evaporation using a shadow mask. The all-gel OECT with a coplanar gate structure was used for the fabrication of sensor array. The semiconducting polymer gel active layer and PIL ionogel electrolyte were coated on the PU substrate with an electrode array via the same spin-coating method to afford an all-gel OECT pressure sensor array.

Structural characterizations

The thickness and morphology of the semiconducting polymer gel active layer were determined using a field emission scanning electron microscope (Nova Nano SEM 450, FEI, USA) and a transmission electron microscope (TEM) (JEM-F200, JEOL, Japan). The morphologies of Ag/Au electrode before and after stretching were observed by an optical microscope (6XB-PC, Shang Guang, P. R. China). The chemical structures of the semiconducting polymer gels with different PEDOT:PSS contents were characterized by a FTIR spectrometer (EQUINOX55, Bruker, Germany) and an XPS (Nexsa, Thermo Scientific, USA). The packing of PEDOT:PSS chains in semiconducting films was investigated by grazing-incidence wide-angle X-ray scattering (GIWAXS) (Xeuss2.0, xenocs, France).

OECT characterization

The transfer and output curves of all-gel OECTs were studied using a semiconductor analyzer (PDA Fs-pro, Primarius, China) and a probe station (Xitatech, China). For the transfer curves, drain voltage (V_D) was maintained at −0.5 V, while it varied between −1.0 and 2.0 V for the output curves. Transconductance curves were derived from the transfer curves. On/off cycling stability of all-gel OECT was investigated by switching V_G between −0.5 V and 1.0 V under a fixed V_D of −0.5 V. Capacitances of typical semiconducting polymer gel films were determined by the electrochemical impedance spectroscopy measured with an electrochemical workstation (CHI600E, CH Instruments, USA). The standard three-electrode (working, reference, and counter electrodes) system was connected to the electrochemical workstation for impedance test. The semiconductor gel active layer was connected to the working electrode, while a platinum metal was connected to the counter electrode. The semiconducting gel active layer, platinum electrode, and the reference electrode were immersed in [THMA][MeSO4] electrolyte for the measurement of impedance. The

experimental impedance data were imported into a NOVA software and fitted to an $R_s(R_p//C_p)W_s$ equivalent circuit model to calculate the film capacitances. R_s and R_p are the resistances of the electrolyte and the film, respectively, while C_p and W_s are the film capacitance and impedance, respectively.

Mechanical tests

The compressive and tensile mechanical properties of the semiconducting polymer gels and PIL ionogels were investigated by a universal testing machine (Lishi (Shanghai) Instruments Co., Ltd., P. R. China). The electrical properties of the semiconducting polymer gels and PIL ionogels upon compression and stretching were recorded by a LCR meter (TH2827, Tonghui Instrument Factory, P. R. China) at a voltage of 1 V and a frequency of 400 Hz.

Pressure sensing tests

The sensing performance of the all-gel OECT pressure sensor was measured by the same semiconductor analyzer and probe station. V_D was kept at −0.5 V for the transfer curves, while it varied between −1.0 to 2.0 V for the output curves. For a single OECT pressure sensor, different weights were applied to the surface of the device, and its pressure sensing performance was investigated by the change of its transfer curve or drain current. The sensing performance of the pressure sensor array fixed on the palm of a bionic hand was investigated by the change of drain current. When a subject was placed on the palm or the bionic hand grasped a subject, the current distributions of the sensor array were measured by the same semiconductor analyzer and probe station.

FEA mechanical simulation

The structure variation and stress/strain distribution of the PIL ionogel electrolyte layer with a pyramid-shaped microstructured surface were simulated by FEA software Abaqus. The compressive elastic modulus of the ionogel model was 69 kPa, while the tensile elastic modulus was 62 kPa. The Poisson's ratio of the ionogel model was 0.45. The width × length × height of the pyramid-shaped microstructure of the ionogel model was $500 \times 500 \times 1000\,\mu m$, and the distance between each microstructure was 300 μm.

Artificial synapse tests

The synaptic characteristics of the all-gel OECT with a coplanar gate structure were studied by the same semiconductor analyzer with a V_D of −15 mV. The presynaptic pulses with different pulse widths, intervals, numbers, and V_G values were generated by the same semiconductor analyzer. During measurement, the initial V_G applied on the synaptic OECT was 0.8 V and ΔV_G was in the range of −0.5 to −0.1 V. The EPSC of the stretched synaptic OECT with 30% tensile strain along the direction perpendicular to channel length was also measured to investigate the stretchability of the synaptic OECT. The learning-forgetting-relearning process was simulated by applying V_G pulses with a pulse width of 50 ms and a pulse interval of 50 ms.

Gas sensing tests

As shown in Supplementary Fig. 28, the self-made gas sensing device is composed of an air inlet, an air outlet, and a 1 L cavity. The all-gel OECT gas sensor was placed in the cavity and connected to the semiconductor analyzer. 200 ppm NH_3 was diluted with air through 10 L gas sampling bags to obtain the required concentrations. The change of drain current of the all-gel OECT gas sensor upon exposure to different concentrations of NH_3 was measured by the same semiconductor analyzer. V_G and V_D were kept at 0.5 V and −0.1 V, respectively, for gas sensing tests. To demonstrate the capability of the all-gel OECT gas sensor in food quality monitoring, a piece of fresh pork with a mass of around 100 g together with the gas sensor were sealed in a glass container and exposed to the sun. The responses of the all-gel OECT gas sensor inside the container after 2–20 days were measured to evaluate the concentration of NH_3 generated from the rotting meat.

Data availability

The data generated in this study are provided in the Manuscript, Supplementary Information, and Source Data file. Source data are provided with this paper.

References

1. Song, J., Liu, H., Zhao, Z., Lin, P. & Yan, F. Flexible organic transistors for biosensing: devices and applications. *Adv. Mater.* **36**, 2300034 (2023).
2. Wang, L. et al. Flexible organic electrochemical transistors for chemical and biological sensing. *Nano Res.* **15**, 2433–2464 (2021).
3. Yao, Y. et al. Flexible and stretchable organic electrochemical transistors for physiological sensing devices. *Adv. Mater.* **35**, 2209906 (2023).
4. Fan, X. et al. PEDOT:PSS for flexible and stretchable electronics: Modifications, strategies, and applications. *Adv. Sci.* **6**, 1900813 (2019).
5. Liu, D. et al. A wearable in-sensor computing platform based on stretchable organic electrochemical transistors. *Nat. Electron.* **7**, 1176–1185 (2024).
6. Lee, Y. et al. Stretchable organic optoelectronic sensorimotor synapse. *Sci. Adv.* **4**, eaat7387 (2018).
7. Huang, B. et al. Skin-like n-type stretchable synaptic transistors with low energy consumption and highly reliable plasticity for brain-inspired computing. *Nano Energy* **128**, 109891 (2024).
8. Peng, Y. et al. Stretchable organic electrochemical transistors via three-dimensional porous elastic semiconducting films for artificial synaptic applications. *Nano Res.* **16**, 10206–10214 (2023).
9. Gu, P. et al. Highly stretchable semiconducting aerogel films for high-performance flexible electronics. *Adv. Funct. Mater.* **34**, 2400589 (2024).
10. Chen, J. et al. Highly stretchable organic electrochemical transistors with strain-resistant performance. *Nat. Mater.* **21**, 564–571 (2022).
11. Li, X. et al. 3D-printed intrinsically stretchable organic electrochemical synaptic transistor array. *ACS Appl. Mater. Interfaces* **15**, 41656–41665 (2023).
12. Liu, K. et al. Low-voltage intrinsically stretchable organic transistor amplifiers for ultrasensitive electrophysiological signal detection. *Adv. Mater.* **35**, 2207006 (2022).
13. Liu, J. et al. Fully stretchable active-matrix organic light-emitting electrochemical cell array. *Nat. Commun.* **11**, 3362 (2020).
14. Kim, C.-H. et al. All-printed and stretchable organic electrochemical transistors using a hydrogel electrolyte. *Nanoscale* **15**, 3263–3272 (2023).
15. Liu, D. et al. Intrinsically stretchable organic electrochemical transistors with rigid-device-benchmarkable performance. *Adv. Sci.* **9**, 2203418 (2022).
16. Zhang, S. et al. Tuning the electromechanical properties of PEDOT:PSS films for stretchable transistors and pressure sensors. *Adv. Electron. Mater.* **5**, 1900191 (2019).
17. Lee, W. et al. Nonthrombogenic, stretchable, active multielectrode array for electroanatomical mapping. *Sci. Adv.* **4**, eaau2426 (2018).
18. Li, J. et al. Tough adhesives for diverse wet surfaces. *Science* **357**, 378–381 (2017).
19. Zhao, X. et al. Soft materials by design: unconventional polymer networks give extreme properties. *Chem. Rev.* **121**, 4309–4372 (2021).
20. Yuk, H., Wu, J. & Zhao, X. Hydrogel interfaces for merging humans and machines. *Nat. Rev. Mater.* **7**, 935–952 (2022).

21. Bai, J. et al. Coin-sized, fully integrated, and minimally invasive continuous glucose monitoring system based on organic electrochemical transistors. *Sci. Adv.* **10**, eadl1856 (2024).

22. Liu, Z. et al. Wireless intelligent patch for closed-loop in situ wound management. *Adv. Sci.* **11**, e2400451 (2024).

23. Li, P. et al. N-type semiconducting hydrogel. *Science* **384**, 557–563 (2024).

24. Fang, B. et al. Scalable production of ultrafine polyaniline fibres for tactile organic electrochemical transistors. *Nat. Commun.* **13**, 2101 (2022).

25. Wang, W. et al. High-transconductance, highly elastic, durable and recyclable all-polymer electrochemical transistors with 3D micro-engineered interfaces. *Nano Micro Lett.* **14**, 184 (2022).

26. Hu, J. et al. Multifunctional hydrogel hybrid-gated organic photo-electrochemical transistor for biosensing. *Adv. Funct. Mater.* **32**, 2109046 (2022).

27. He, R. et al. Organic electrochemical transistor based on hydrophobic polymer tuned by ionic gels. *Angew. Chem. Int. Ed.* **62**, e202304549 (2023).

28. Tseng, A. C. & Sakata, T. Direct electrochemical signaling in organic electrochemical transistors comprising high-conductivity double-network hydrogels. *ACS Appl. Mater. Interfaces* **14**, 24729–24740 (2022).

29. Dai, Y. et al. Soft hydrogel semiconductors with augmented biointeractive functions. *Science* **386**, 431–439 (2024).

30. Su, X. et al. A highly conducting polymer for self-healable, printable, and stretchable organic electrochemical transistor arrays and near hysteresis-free soft tactile sensors. *Adv. Mater.* **34**, 2200682 (2022).

31. Zhou, X. et al. Aerosol jet printing of multi-dimensional OECT force sensor with high sensitivity and large measuring range. *Adv. Mater. Technol.* **8**, 2201272 (2023).

32. Chen, S., Surendran, A., Wu, X. & Leong, W. L. Contact modulated ionic transfer doping in all-solid-state organic electrochemical transistor for ultra-high sensitive tactile perception at low operating voltage. *Adv. Funct. Mater.* **30**, 2006186 (2020).

33. Yin, Y. et al. In-sensor organic electrochemical transistor for the multimode neuromorphic olfactory system. *ACS Sens.* **9**, 4277–4285 (2024).

34. Deng, Y. et al. A flexible and biomimetic olfactory synapse with gasotransmitter-mediated plasticity. *Adv. Funct. Mater.* **33**, 2214139 (2023).

35. Chouhdry, H. H., Lee, D. H., Bag, A. & Lee, N.-E. A flexible artificial chemosensory neuronal synapse based on chemoreceptive ionogel-gated electrochemical transistor. *Nat. Commun.* **14**, 821 (2023).

36. Mellein, B. R., Scurto, A. M. & Shiflett, M. B. Gas solubility in ionic liquids. *Curr. Opin. Green. Sustain. Chem.* **28**, 100425 (2021).

37. Jin, M. L. et al. Scalable superior chemical sensing performance of stretchable ionotronic skin via a π-hole receptor effect. *Adv. Mater.* **33**, e2007605 (2021).

38. Zhang, X. et al. Bioinspired gradient poly(ionic liquid) ionogels for ionic skins with an ultrawide pressure detection range. *ACS Mater. Lett.* **4**, 2459–2468 (2022).

39. Won, D. et al. Laser-induced wet stability and adhesion of pure conducting polymer hydrogels. *Nat. Electron.* **7**, 475–486 (2024).

40. Hu, Z. et al. Nanoporous conjugated polymer aerogel films for high-performance electrochemical transistors. *Adv. Funct. Mater.* **34**, 2410788 (2024).

41. Zhang, X. et al. Stretchable and negative-poisson-ratio porous metamaterials. *Nat. Commun.* **15**, 392 (2024).

42. Fan, W. et al. An antisweat interference and highly sensitive temperature sensor based on poly(3,4-ethylenedioxythiophene)-poly(-styrenesulfonate) fiber coated with polyurethane/graphene for real-time monitoring of body temperature. *ACS Nano* **17**, 21073–21082 (2023).

43. Lehane, R. A. et al. Electrosynthesis of biocompatible free-standing PEDOT thin films at a polarized liquid|liquid interface. *J. Am. Chem. Soc.* **144**, 4853–4862 (2022).

44. Chen, G. et al. Strain-and strain-rate-invariant conductance in a stretchable and compressible 3D conducting polymer foam. *Matter* **1**, 205–218 (2019).

45. Zu, G., Zeng, S., Yang, B. & Huang, J. Transparent, ultraflexible, and superinsulating nanofibrous biocomposite aerogels via ambient pressure drying. *J. Mater. Chem. A* **9**, 5769–5779 (2021).

46. Huang, L. et al. Porous semiconducting polymers enable high-performance electrochemical transistors. *Adv. Mater.* **33**, 2007041 (2021).

47. Wu, X. et al. Ionic-liquid induced morphology tuning of PEDOT:PSS for high-performance organic electrochemical transistors. *Adv. Funct. Mater.* **32**, 2108510 (2022).

48. Wang, L. et al. Realizing ultrahigh transconductance in organic electrochemical transistor by co-doping PEDOT: PSS with ionic liquid and dodecylbenzenesulfonate. *Macromol. Rapid Commun.* **43**, 2200212 (2022).

49. Dai, S. et al. Intrinsically stretchable neuromorphic devices for on-body processing of health data with artificial intelligence. *Matter* **5**, 3375–3390 (2022).

50. Xu, Y. et al. Stretchable and neuromorphic transistors for pain perception and sensitization emulation. *Mater. Horiz.* **11**, 958–968 (2024).

51. Cao, Y. et al. Self-healing electronic skins for aquatic environments. *Nat. Electron.* **2**, 75–82 (2019).

52. Zhang, X. et al. Bioinspired gradient stretchable aerogels for ultrabroad-range-response pressure-sensitive wearable electronics and high-efficient separators. *Angew. Chem. Int. Ed.* **62**, e202213952 (2023).

53. Bernards, D. A. & Malliaras, G. G. Steady-state and transient behavior of organic electrochemical transistors. *Adv. Funct. Mater.* **17**, 3538–3544 (2007).

54. Gao, Y. et al. A hybrid transistor with transcriptionally controlled computation and plasticity. *Nat. Commun.* **15**, 1598 (2024).

55. Harikesh, P. C. et al. Organic electrochemical neurons and synapses with ion mediated spiking. *Nat. Commun.* **13**, 901 (2022).

56. Dai, S. et al. Recent advances in transistor-based artificial synapses. *Adv. Funct. Mater.* **29**, 1903700 (2019).

57. Xia, P. et al. Designing a redox heterojunction for photocatalytic "overall nitrogen fixation" under mild conditions. *Adv. Mater.* **34**, e2200563 (2022).

58. Zhang, J. et al. Retina-inspired artificial synapses with ultraviolet to near-infrared broadband responses for energy-efficient neuromorphic visual systems. *Adv. Funct. Mater.* **33**, 2302885 (2023).

59. Zhang, J. et al. Tailoring neuroplasticity in flexible perovskite QDs-based optoelectronic synaptic transistors by dual modes modulation. *Nano Energy* **95**, 106987 (2022).

60. Guo, Z. et al. Optoelectronic synapses and photodetectors based on organic semiconductor/halide perovskite heterojunctions: materials, devices, and applications. *Adv. Funct. Mater.* **33**, 2305508 (2023).

61. Qin, C. et al. Artificial olfactory biohybrid system: an evolving sense of smell. *Adv. Sci.* **10**, e2204726 (2023).

62. Gkoupidenis, P., Schaefer, N., Garlan, B. & Malliaras, G. G. Neuromorphic functions in PEDOT:PSS organic electrochemical transistors. *Adv. Mater.* **27**, 7176–7180 (2015).

63. Zhou, B. et al. Organic electrochemical transistors toward synaptic electronics. *J. Phys. D Appl. Phys.* **55**, 304006 (2022).

64. Lei, Z., Dai, C. & Chen, B. Gas solubility in ionic liquids. *Chem. Rev.* **114**, 1289–1326 (2014).

65. Siribunbandal, P., Osotchan, T., Kim, Y.-H. & Jaisutti, R. Highly sensitive colorimetric ammonia sensors based on polydiacetylene/zinc oxide nanopellet-embedded PDMS films for meat spoilage detection. *ACS Appl. Polym. Mater.* **5**, 7786–7794 (2023).

66. Matsuhisa, N. et al. High-transconductance stretchable transistors achieved by controlled gold microcrack morphology. *Adv. Electron. Mater.* **5**, 1900347 (2019).

67. Dai, Y. H. et al. Stretchable redox-active semiconducting polymers for high-performance organic electrochemical transistors. *Adv. Mater.* **34**, 2201178 (2022).

68. Demuru, S. et al. Antibody-coated wearable organic electrochemical transistors for cortisol detection in human sweat. *ACS Sens.* **8**, 940 (2023).

69. Lee, S.-K. et al. Nanofiber channel organic electrochemical transistors for low-power neuromorphic computing and wide-bandwidth sensing platforms. *Adv. Sci.* **8**, 2001544 (2021).

70. Pappa, A.-M. et al. Organic transistor arrays integrated with finger-powered microfluidics for multianalyte saliva testing. *Adv. Healthc. Mater.* **5**, 2295–2302 (2016).

71. Hopkins, J. et al. A phosphonated poly(ethylenedioxythiophene) derivative with low oxidation potential for energy-efficient bioelectronic devices. *Chem. Mater.* **34**, 140–151 (2022).

72. Li, T. et al. Biocompatible ionic liquids in high-performing organic electrochemical transistors for ion detection and electrophysiological monitoring. *ACS Nano* **16**, 12049–12060 (2022).

73. Cea, C. et al. Enhancement-mode ion-based transistor as a comprehensive interface and real-time processing unit for in vivo electrophysiology. *Nat. Mater.* **19**, 679–686 (2020).

74. Yan, Y. et al. High-performance organic electrochemical transistors with nanoscale channel length and their application to artificial synapse. *ACS Appl. Mater. Interfaces* **12**, 49915–49925 (2020).

75. Stephen, M. et al. Crown ether enabled enhancement of ionic-electronic properties of PEDOT:PSS. *Mater. Horiz.* **9**, 2408–2415 (2022).

76. Taussig, L. et al. Electrostatic self-assembly yields a structurally stabilized PEDOT:PSS with efficient mixed transport and high-performance OECTs. *Matter* **7**, 1071–1091 (2024).

77. Donahue, M. J. et al. High-performance vertical organic electrochemical transistors. *Adv. Mater.* **30**, 1705031 (2018).

78. Spyropoulos, G. D., Gelinas, J. N. & Khodagholy, D. Internal ion-gated organic electrochemical transistor: a building block for integrated bioelectronics. *Sci. Adv.* **5**, eaau7378 (2019).

79. Wu, M. et al. Stretchable, skin-conformable neuromorphic system for tactile sensory recognizing and encoding. *InfoMat* **5**, 2770–5110 (2023).

80. Kim, D. W., Yang, J. C., Lee, S. & Park, S. Neuromorphic processing of pressure signal using integrated sensor-synaptic device capable of selective and reversible short- and long-term plasticity operation. *ACS Appl. Mater. Interfaces* **12**, 23207–23216 (2020).

Acknowledgements

Author contributions

L.L. carried out most of the experiments, analyzed the data, and drafted the paper. X. Liu revised the manuscript. Z.H. and P.G. provided data analysis. Z.D., X. Liang, and Z.S. provided experimental support. X.Z. and X.Y. conducted background research and revised the paper. G.Z. proposed the concept, revised the manuscript, and supervised the research. J.Y. and J.H. revised the manuscript and supervised the research. All authors contributed to discussing and revising the manuscript.

Competing interests

The authors declare no competing interests.

Additional information

Supplementary information The online version contains supplementary material available at https://doi.org/10.1038/s41467-025-59240-0.

Correspondence and requests for materials should be addressed to Jie Yang, Guoqing Zu or Jia Huang.

Peer review information *Nature Communications* thanks Wei Huang, and the other, anonymous, reviewer(s) for their contribution to the peer review of this work. A peer review file is available.

Reprints and permissions information is available at http://www.nature.com/reprints

Publisher's note Springer Nature remains neutral with regard to jurisdictional claims in published maps and institutional affiliations.